Visual-LiDAR Odometry for Planetary Rover with Plane Constraints

Lingxiao Zhang[1], Rong Huang[1,2], Yusheng Xu[1,2], Zhen Ye[1,2], Changjiang Xiao[1,2], Xiaohua Tong[1,2]

[1] College of Surveying and Geo-Informatics, Tongji University, Shanghai, China
[2] Shanghai Key Laboratory for Planetary Mapping and Remote Sensing for Deep Space Exploration, Shanghai, China

Keywords: Planetary rover, Extraterrestrial surfaces, Visual-LiDAR Odometry, Plane Constraints.

Abstract

In space exploration missions, planetary rovers require precise navigation to ensure operational safety and efficiency. This paper presents a novel visual-LiDAR odometry method designed specifically for planetary rovers, aiming to address the challenges of accurate navigation in planetary environments that are GNSS-denied and characterized by low texture and unstructured surfaces. By combining visual information from a monocular camera with the high-precision geometric measurements of the LiDAR sensor, the system is capable of achieving accurate localization and pose estimation in a planetary-like scenario. Furthermore, the incorporation of ground segmentation for the LiDAR point cloud and the application of ground plane constraints can effectively alleviate the attitude drift during the motion process, thereby enhancing the overall accuracy. Experimental results on the Erfoud dataset show that the proposed system achieves positioning accuracies (i.e., absolute trajectory error) of 3.334% and 3.869% over the full trajectory length of two sequences, outperforming state-of-the-art methods. This research provides a promising solution for the autonomous navigation of planetary rovers in complex environments.

1. Introduction

Planetary rovers play a pivotal role in space exploration, enabling in-situ scientific data acquisition, geological analysis, and the search for extraterrestrial life (Wang et al., 2017). Most planetary missions have successfully deployed rovers for geological surveys and sampling (Lai et al., 2020). Precise navigation and localization are critical for rovers. However, the absence of a Global Navigation Satellite System (GNSS) and significant communication delays with Earth pose substantial challenges to real-time high-precision positioning (Kaichang et al., 2018). Consequently, rovers rely on autonomous navigation systems for path planning and obstacle avoidance in unknown environments, ensuring safe and efficient exploration.

Dead reckoning (DR), utilizing Inertial Measurement Units (IMU) and wheel odometers, is widely adopted in planetary rovers (Green and Sasiadek, 1998). However, drift errors are accumulated over long distances using IMU as odometry, and the loose soil and rugged terrain of planetary surfaces often cause wheel slippage, reducing accuracies of DR to approximately 10% of the traveled distance (Ali et al., 2005, Jia et al., 2022, Sicong et al., 2022). In recent years, Visual Odometry (VO) has been employed in rovers, achieving higher localization accuracy through feature matching and tracking in camera images (Andolfo et al., 2022, Maimone et al., 2007). VO systems enhanced with optimization and mapping modules are referred to as Visual Simultaneous Localization and Mapping (SLAM), which performs loop closure and global optimization to correct accumulated errors, maintaining long-term accuracy (Cheng et al., 2022, Xia et al., 2021). These features make VO and SLAM prominent techniques in autonomous rover navigation.

Planetary surfaces, characterized by low texture and significant illumination variations, present challenges for visual sensors, including feature extraction errors, inaccurate depth estimation, and unreliable terrain mapping in low-contrast scenes. These challenges are exacerbated in key exploration areas, such as the Moon’s south pole, where permanently shadowed regions (PSRs) lack direct sunlight, rendering optical cameras ineffective for navigation (Brown et al., 2022). Light Detection and Ranging (LiDAR) systems, unaffected by lighting conditions, provide high-precision 3D coordinates and real-time dense point cloud maps, offering significant advantages for obstacle detection and navigation (Guo et al., 2022, Li et al., 2024). LiDAR has been utilized for precise planetary landings and is considered essential for exploring PSRs (Cremons, 2022). However, the largely unstructured planetary surfaces often lack sufficient geometric features, leading to the degeneracy of LiDAR-only systems in open and unstructured environments (Ebadi et al., 2023). Moreover, planetary rover trajectories rarely form loops, making SLAM loop closure ineffective and computationally costly (Xia et al., 2023). Consequently, odometry is mainly used for short-range navigation due to its weakness in dealing with long-distance localization.

Visual-LiDAR fusion odometry integrates the advantages of both sensors and has demonstrated remarkable robustness and accuracy in terrestrial environments (Zhu et al., 2023). Nevertheless, achieving comparable performance under feature-sparse planetary conditions remains a significant research challenge. To address these limitations, this study proposes a visual-LiDAR fusion odometry method tailored for extreme planetary environments, which takes full advantage of the complementary strengths of a monocular RGB camera and LiDAR, enhances the robustness and reliability of the system, and achieves stable and accurate autonomous positioning.

The main contributions of this paper are summarized as follows:

- We propose a monocular camera-LiDAR fusion odometry pipeline for high-precision rover localization, validated on the Erfoud planetary simulation dataset.
- Through ground constraints between LiDAR point clouds and tight coupling between multiple sensors, sensor degeneracy in unstructured planetary environments is suppressed, and vertical trajectory drift is effectively reduced.

2. Related Work

2.1 Localization Methods for Planetary Rovers

Global localization directly determines the absolute position of the rover on a global map (Tian et al., 2024). Celestial navigation is the most straightforward global localization method, using solar sensors or star trackers to determine the direction of the Sun or the positions of stars for localization (Yang et al., 2014). Another solution is to utilize satellite communication for global localization, where an orbiter maintains a connection with the rover to achieve precise positioning (Jun et al., 2022). The matching of Planetary Remote Sensing Images (PRSI) can also be used for the navigation and positioning of rovers, but it requires more computing resources and time (Wan et al., 2025). Landmark-based matching is another representative approach, where the rover's acquired data is matched with global information provided by orbiters or satellites for localization (Daftry et al., 2023). Lunar or Martian craters are the most commonly used landmarks, and their recognition in images enables navigation when matched with satellite maps (Ye et al., 2025). At present, multi-source remote sensing image-matching technologies in the field of planetary exploration have begun to attract widespread attention (Huang et al., 2024). Some researchers have also proposed suggestions for cooperation between rovers and orbiters to improve the accuracy of VO. (Sasaki et al., 2020). However, this method does not provide the detailed information required for accurate navigation and is dependent on communications between the Earth and the rover.

Relative localization determines the rover's position by computing its cumulative motion between consecutive frames. In planetary rover missions, the accuracy of wheel odometry is often affected by wheel slippage; therefore, it is typically combined with IMU to enhance accuracy and reliability (Kaichang et al., 2021). VO estimates motion based on 3D geometric structures obtained from stereo images rather than velocity measurements, determining the rover's movement relative to its starting position (Maimone et al., 2007). However, in feature-sparse planetary terrains, this method is prone to accumulating localization errors. Moreover, harsh lighting conditions, low-texture environments, and hardware constraints further exacerbate error accumulation challenges (Harrell et al., 2021).

2.2 Visual-LiDAR Odometry

By integrating the rich texture information from visual sensors with the high-precision depth perception of LiDAR, visual-LiDAR-based odometry methods significantly enhance system robustness and localization accuracy (Wu et al., 2021), particularly in planetary environments with poor lighting conditions and sparse textures (Xie et al., 2023). DEMO (Zhang et al., 2017), a depth-enhanced VO method, fused depth information to improve localization accuracy while maintaining real-time processing capabilities. LIMO (LiDAR-Monocular Odometry) (Graeter et al., 2018) combined LiDAR point clouds and monocular images to achieve robust VO, demonstrating good adaptability in sparse observation environments. Beyond point cloud-based approaches, geometric primitives such as lines can also be used in monocular VO to enhance localization performance in complex environments (Huang et al., 2020). By integrating depth features and loop closure detection, tightly coupled visual-LiDAR odometry methods significantly improve accuracy and robustness in dynamic and uncertain environments (Meng et al., 2022). These studies provide strong evidence for the feasibility of visual-LiDAR odometry methods in planetary rover navigation under complex space conditions. However, existing visual-LiDAR odometry systems designed for terrestrial urban environments fail to adequately address two critical challenges in feature-sparse, unstructured planetary surface scenarios: cumulative drift and sensor degeneracy (Chiodini et al., 2021, Li et al., 2022). SLAM usually employs loop closure to correct accumulated errors. However, planetary rovers seldom backtrack their paths, thereby limiting the applicability of this method (Kaichang et al., 2021). Furthermore, due to inherent computational limitations in space systems and stringent certification procedures, SLAM has not yet been applied in actual space missions (Geromichalos et al., 2020).

3. Methodology

The proposed fusion-based odometry method consists of a depth-enhanced VO module and a ground-constraints LiDAR odometry (LO) module, as shown in Figure 1.

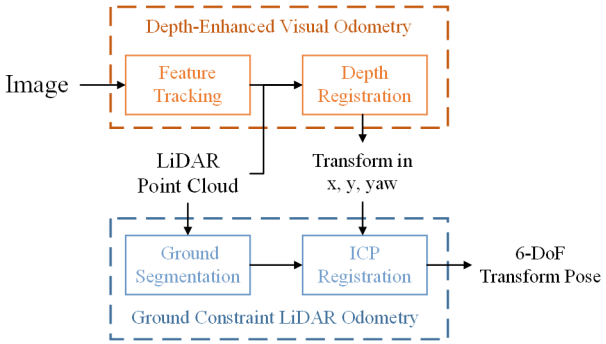

Figure 1. Flowchart of the proposed pipeline.

To address sensor degeneracy and odometry drift issues in the weakly textured, unstructured environment of planetary surfaces, we propose an improved approach that achieves low-drift, 6 degree-of-freedom (DOF) pose estimation. The visual-LiDAR odometry module receives images I_k and LiDAR point clouds P_k as inputs. Through feature extraction and matching, image feature points between adjacent frames I_k and I_{k-1} are tracked to estimate the changes in x, y displacements, and yaw angle. The LiDAR point cloud P_k undergoes ground segmentation to obtain the ground plane point cloud P_k^{gr}. Fusing the x, y displacement and yaw angle estimates from VO, the z, $pitch$, and $roll$ angle variations are estimated by registering P_k^{gr} with P_{k-1}^{gr}, resulting in the complete frame-to-frame transformation T_{k-1}^{k}.

3.1 Depth-Enhanced Visual Odometry

On planetary surfaces, the lack of significant textures makes it highly challenging to accurately reconstruct pixel depths through disparity and triangulation, especially when using monocular cameras, as in the proposed system. To overcome this, we leverage the high-precision distance measurement capabilities of the LiDAR sensor. By applying the intrinsic matrix K of the camera and extrinsic transformation T_L^C between the LiDAR coordinate system L and the camera coordinate system C, using Eq. 1 we project the LiDAR point cloud into the image frame to generate a depth map.

$$P_k^I = K \cdot T_L^C \cdot P_k^L \tag{1}$$

where P_k^L represents the 3D coordinates of the LiDAR point cloud in the LiDAR coordinate system, and P_k^I is the 3D coordinates of the LiDAR point cloud in the image coordinate system, with the z-axis value representing the pixel depth. Through this projection, we combine the high-precision depth information from LiDAR with the image features, generating a depth-enhanced VO system. Figure. 2 illustrates an example of projecting LiDAR points onto the image plane coordinate of the corresponding camera frame.

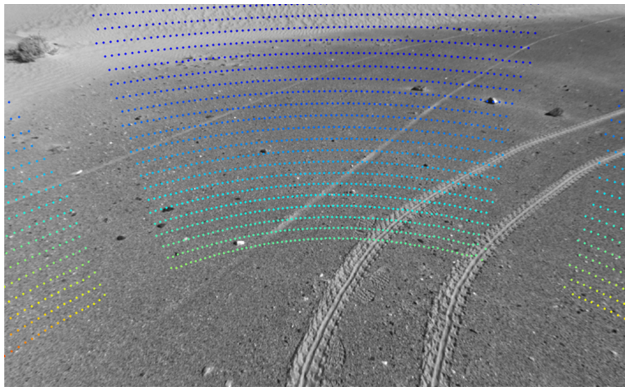

Figure 2. Illustration of LiDAR point cloud projection onto the image plane.

For the same feature point X_i in k frames (X_i^k) and $k-1$ (X_i^{k-1})there are:

$$X_i^k = \mathbf{R}_{k-1}^k X_i^{k-1} + \mathbf{t}_{k-1}^k \tag{2}$$

where $\mathbf{R}_{k-1}^k$ is the rotation matrix between adjacent frames, and $\mathbf{t}_{k-1}^k$ is the translation vector, transformation$\mathbf{T}_{k-1}^k = (\mathbf{R}_{k-1}^k|\mathbf{t}_{k-1}^k)$. Subsequently, we use nonlinear least squares optimization to estimate the pose transformation:

$$\min_{\mathbf{R}_{k-1}^k, \mathbf{t}_{k-1}^k} (\sum_i \left\| X_i^k - \mathbf{R}_{k-1}^k X_i^{k-1} + \mathbf{t}_{k-1}^k \right\|^2) \tag{3}$$

By Eq.3, we get the optimal transform between adjacent frames.

3.2 Ground-constraints LiDAR Odometry

Although LiDAR point clouds provide high-precision depth information, the point densities are low, especially in the vertical direction. In unstructured environments with a lack of vertical features, there can be substantial depth differences between adjacent LiDAR points. This leads to considerable pose drift along the z-axis, $roll$ and $pitch$ directions when using VO. To address this issue, we introduce ground-plane constraints for LiDAR point clouds. We adopted the idea of LEGO-LOAM (Shan and Englot, 2018) and utilized the ground plane information. Firstly, we performed clustering and segmentation on the collected point cloud to separate the ground point cloud P^{gr} and filter out the abnormal points. We treat the entire ground plane as a unified feature rather than extracting individual feature points. Figure. 3 illustrates the schematic diagram of ground point cloud segmentation for a single frame of LiDAR point cloud.

For each point P_i^{gr} on the ground plane, we construct a point-to-plane residual and directly estimate the optimal pose transformation $\mathbf{T}$ using the ICP (Iterative Closest Point) algorithm, as defined in Eq. 4.

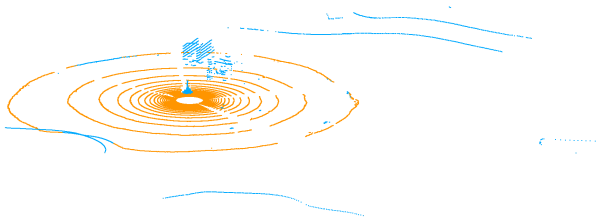

Figure 3. Illustration of the ground segmentation result of LiDAR point cloud. The yellow points represent the segmented ground points.

$$\min_{\mathbf{T}_{k-1}^k} \sum_{i=1}^{n} \| P_{k,i}^{gr} - \mathbf{T}_{k-1}^k P_{k-1,i}^{gr} \|^2 \tag{4}$$

where $P_{k,i}^{gr}$ and $P_{k-1,i}^{gr}$ are the i-th points from the ground-plane point clouds in the current and previous frames, respectively, and $\mathbf{T}_{k-1}^k$ is the pose transformation between the frames k and $k-1$. When vertical drift occurs, the point-to-plane distance undergoes significant changes, providing an effective constraint in the vertical direction. Furthermore, since feature point extraction is not required, this approach reduces computational complexity and improves processing efficiency, making it more suitable for planetary rovers with limited computational resources. In this process, the initial value of $\mathbf{T}_{k-1}^k$ is obtained from the VO module, as described in Eq. 3.

It is important to note that during the solution of Eq. 4, only the vertical components of $\mathbf{T}_{k-1}^k$ (i.e., z, $roll$, and $pitch$) are iteratively optimized, while the horizontal components (i.e., x, y, and yaw) are kept fixed. This is because, on planetary surfaces, the environment is vast and featureless, resulting in weak horizontal constraints from the LiDAR sensor, which can lead to catastrophic drift in the horizontal pose components, a phenomenon known as degeneracy. Therefore, with this specially customized pose coupling strategy, we use ground-plane constraints to optimize only the vertical component of the VO result, avoiding degeneracy while improving positioning accuracy.

4. Experiments

4.1 Experimental Dataset

We use the Erfoud dataset (Lacroix et al., 2020) to evaluate the performance of the proposed method. This dataset was collected at three Mars-analog sites in the Tafilalet region of Morocco. We selected two sequences recorded using a stereo navigation camera and a Velodyne HDL-32 LiDAR: Trajectory21re1 and Trajectory22re3, with travel distances of 622.071 m and 919.628 m, respectively. These distances exceed the autonomous driving ranges of all the landed planetary rovers, providing an ideal test case for validating our method. Since our visual module is based on monocular vision, we only use images from the left camera. The environment in the Erfoud

dataset closely resembles the actual Martian landscape (Figure 4), characterized by low texture, open, and unstructured terrain, making it well-suited for the needs of our research.

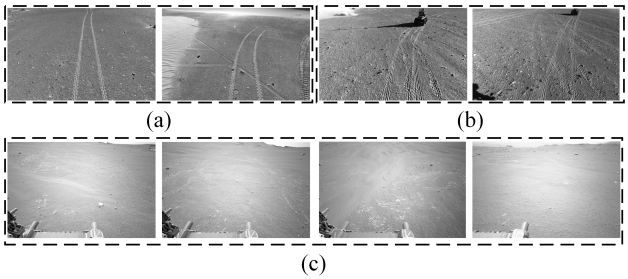

Figure 4. The Erfoud dataset collection environment compared to the actual Martian landscape. (a) shows the scene in Trajectory21re1. (b) shows the scene in Trajectory22re3. (c) shows a real Martian image captured by the “Perseverance” rover, which successfully landed on Mars in 2021.

4.2 Evaluation Criteria

4.2.1 Odometry Trajectory Evaluation To assess the accuracy of a SLAM system, we evaluate its performance by comparing the estimated trajectory with the ground truth trajectory. The Absolute Trajectory Error (ATE) is adopted as the primary metric to quantify the deviation between the estimated trajectory and the ground truth at the same timestamp. The Root Mean Square Error (RMSE) of ATE is used to summarize the overall trajectory deviation. Specifically, for the i-th frame, the ATE RMSE is defined as:

$$\text{ATERMSE} = \sqrt{\frac{1}{N}\sum_{i=1}^{N} \|\mathbf{t}_i^{\text{est}} - \mathbf{t}_i^{\text{gt}}\|^2} \tag{5}$$

where N is the total number of frames, and $\mathbf{t}_i^{\text{est}}$ and $\mathbf{t}_i^{\text{gt}}$ denote the estimated and ground truth translational components of the i-th frame, respectively.

4.2.2 Degeneracy Evaluation Degeneracy in odometry systems refers to situations where the system fails to fully constrain the optimization problem, leading to unreliable pose estimates. Current methods for detecting degeneracy are primarily based on analyzing the properties of the Hessian Matrix used in nonlinear least-squares optimization. Some researchers proposes using the minimum eigenvalue (λ_{min}) of the Hessian matrix as an indicator of degeneracy (Zhang et al., 2016). They argue that a smaller λ_{min} suggests a higher likelihood of degeneracy, as it implies that the system is less constrained in certain directions. Although this method is intuitive, other researchers points out that the physical interpretation of eigenvalues is often unclear, and their measurement can be challenging in practice (Zhen and Scherer, 2019). Moreover, the eigenvalue-based methods for detecting degeneracy in LiDAR systems are limited due to their sensitivity to environmental factors, such as measurement noise and the number of valid points in point cloud registration. Therefore, the current mainstream idea is to use the condition number ($\kappa(\mathbf{H})$) of the Hessian matrix to evaluate degeneracy (Hinduja et al., 2019).

$$\kappa(\mathbf{H}) = \frac{\lambda_{\text{max}}}{\lambda_{\text{min}}} \tag{6}$$

where λ_{max} and λ_{min} are the maximum and minimum eigenvalues of the Hessian matrix $\mathbf{H}$, respectively. A larger condition number indicates a higher likelihood of degeneracy. Compared to the single eigenvalue detection method, the condition number approach emphasizes the overall conditioning of the optimization problem, making degeneracy more pronounced while reducing the influence of environmental variables, such as noise and point cloud density.

5. Experimental Result

To comprehensively evaluate the performance of the proposed algorithm, we conducted comparative experiments on the Erfoud dataset against VLOAM (Zhang and Singh, 2015), a representative visual-LiDAR fusion SLAM algorithm known for its strong performance in terrestrial environments. Table 1 presents the RMSE of the ATE for both methods on the Erfoud dataset, while Figure 5 illustrates the estimated trajectories on the Trajectory21re1 and Trajectory22re3 sequences. The experimental results show that the proposed algorithm achieves lower ATE RMSE values on the two sequences, which are 20.739m and 35.584m respectively. Compared with the full length of the ground truth trajectory, the errors are only 3.334% and 3.869% respectively, which is significantly better than VLOAM. The ATE RMSE of VLOAM is 57.417m and 246.531m respectively, and the errors reach 9.230% and 26.808% of the trajectory length. For planetary exploration missions, this is completely unacceptable level of accuracy. The performance gap is largely attributed to the challenges posed by large-scale, open, and flat environments, where LiDAR point clouds exhibit a concentric circular distribution with minimal geometric features and weak curvature variations. This makes it difficult to accurately extract edge and flat points, when enforcing feature extraction would result in high noise levels in the feature extraction results. As shown in Figure 6, even though the motion between consecutive frames is extremely small and the distribution structure of the point cloud remains almost the same, the extracted features are inconsistent, and a large number of feature points that do not actually correspond to each other are forced to be matched, which brings a large amount of error to the feature matching. If this phenomenon is to be ameliorated, sufficient a prior information is needed to continuously adjust the parameters of the feature extraction and matching process, which is difficult to achieve in real planetary exploration missions.

Table 1. Comparison of the localization accuracy of different odometry methods with ATE RMSE (m) using the Erfound dataset.

	VLOAM	Ours
Trajectory21re1	57.417	**20.739**
Trajectory22re3	246.531	**35.584**

VLOAM was able to maintain the approximate shape of the trajectory similar to the ground truth during the initial phase of the Trajectory21re1 sequence, despite the inaccuracy of the estimated rover’s position. However, the effectiveness of its initial attitude guidance diminishes as VO drift accumulates, eventually leading to the degeneracy of the system at a later stage. In the Trajectory22re3 sequence, an abrupt turn at the beginning prevented the VO from providing effective guidance, leading to a noticeable degeneracy directly across the trajectory. By leveraging the superior horizontal constraints of VO, our system guides LO in estimating horizontal poses, thereby enhancing localization accuracy. Figure 7 illustrates the distribution

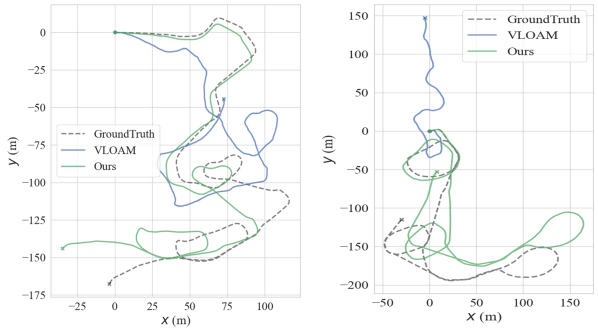

Figure 5. Results of trajectory estimation from different odometry methods in Erfoud dataset. (a) is Trajectory21re1. (b) is Trajectory22re3.

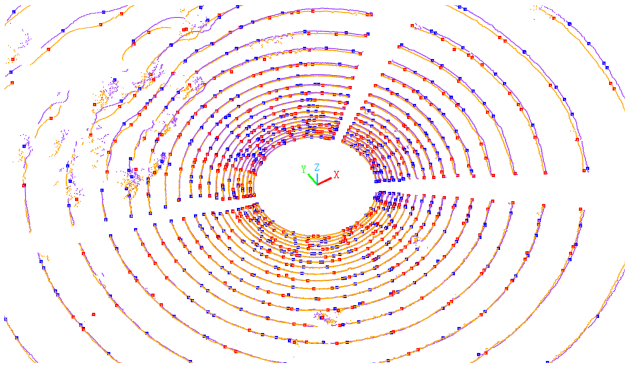

Figure 6. The figure shows LiDAR point distribution in the Erfoud dataset and feature extraction results from VLOAM. Orange and purple points represent current and previous frame LiDAR points, while large red and blue points denote their respective feature points. Despite minimal motion between frames, the feature extractions are significantly different.

of the Hessian matrix condition number before and after applying the visual-LiDAR pose fusion in the nonlinear least squares optimization of LO. Results indicate a significant reduction in condition numbers, from 38.73–495.46 to 6.67–60.55 on Trajectory21re1, and from 56.25–408.30 to 37.46–16.20 on Trajectory22re3. This demonstrates that the multi-sensor fusion effectively mitigates odometry degeneracy between frames, significantly improving system robustness.

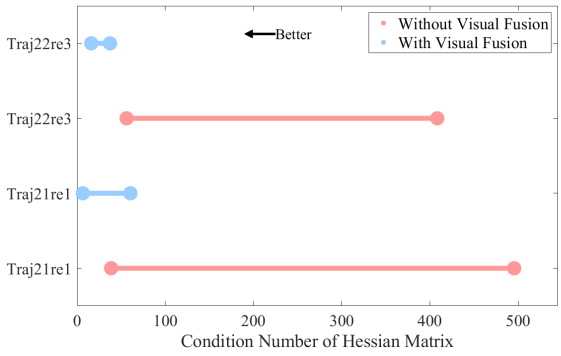

Figure 7. Condition number of the hessian matrix with and without visual fusion.

Additionally, the introduction of ground plane constraints effectively suppresses pose drift in the z-axis, $roll$, and $pitch$ directions for depth-enhanced VO. By treating the entire ground plane as a single feature and constructing point-to-plane residuals, the system provides strong vertical constraints, as any vertical drift results in a noticeable change in point-to-plane distances. Table 2 shows the RMSE of drift along the z-axis direction relative to the ground truth, which visually demonstrates the effectiveness of the ground-plane point cloud constraints in suppressing vertical pose drift in depth-enhanced VO. The ”Without Constraints” results are derived from the pose estimation obtained through depth-enhanced VO (Eq. 3), while the ”With Constraints” results are obtained from the final pose estimation (Eq. 4), with the calculation method following Eq. 5. As seen, the ground-plane constraints effectively limit the drift in the vertical direction within a reasonable range. Specifically, with the ground-plane point cloud constraints, the vertical drift in Trajectory21re1 decreases from 40.730 m to 2.168 m, a reduction of approximately 95%. Similarly, in Trajectory22re3, the drift decreases from 46.120 m to 3.421 m, a reduction of about 93%. These results clearly demonstrate the significant impact of the ground-plane constraints. These findings validate the effectiveness of our point cloud ground segmentation and constraints in reducing vertical drift, ensuring that the cumulative error across the entire trajectory remains within an acceptable range.

Table 2. The localization results of methods with and without ground constraints with RMSE (m) in z-axis using the Erfound dataset.

	Without constraints	With constraints
Trajectory21re1	40.730	**2.168**
Trajectory22re3	46.120	**3.421**

Experimental results indicate that existing SLAM systems face two major challenges in planetary surface environments: (1) LO degeneracy in large-scale, open scenes due to sparse features; and (2) VO suffers from unstable feature tracking in low-texture environments. The proposed algorithm effectively addresses these issues through tightly coupled visual-LiDAR fusion and planar constraints. Specifically, LO utilizes ground plane features to provide vertical constraints, while VO enhances the horizontal constraints, mitigating the random drift in LO. Although the proposed algorithm demonstrates excellent performance on the Erfoud dataset, certain limitations remain. Future improvements include reducing computational overhead to achieve a more lightweight system, integrating multi-sensor data into a joint back-end optimization framework to enhance robustness and localization accuracy, and reconstructing maps of the exploration scene for planetary rover obstacle avoidance. This study demonstrates the system’s strong potential for real-world deployment in planetary rover navigation and localization tasks. Further research will focus on translating this potential into practical applications.

6. Conclusion

We propose a visual-LiDAR fusion odometry method specifically designed for planetary environments. By incorporating ground-plane constraints from LiDAR point clouds, the method effectively suppresses pose drift in planetary rovers operating on weakly textured and open, unstructured terrains. By closely integrating the horizontal constraints from VO measurements

with the vertical constraints from LO measurements, effectively addressing the problem of sensor degeneracy, and significantly enhancing the robustness of the system. Experiments on the Erfoud dataset, a planetary surface simulation environment, validate the effectiveness of the proposed improvements and confirm the algorithm's applicability to planetary surface scenarios. This research provides strong technical support for the autonomous navigation and localization of planetary rovers, showing substantial potential for future applications in space exploration.

References

Ali, K. S., Vanelli, C. A., Biesiadecki, J. J., Maimone, M. W., Cheng, Y., San Martin, A. M., Alexander, J. W., 2005. Attitude and position estimation on the mars exploration rovers. *2005 IEEE International Conference on Systems, Man and Cybernetics*, 1, IEEE, 20–27.

Andolfo, S., Petricca, F., Genova, A., 2022. Visual odometry analysis of the NASA Mars 2020 Perseverance rover's images. *2022 IEEE 9th International Workshop on Metrology for AeroSpace (MetroAeroSpace)*, IEEE, 287–292.

Brown, H., Boyd, A., Denevi, B., Henriksen, M., Manheim, M., Robinson, M., Speyerer, E., Wagner, R., 2022. Resource potential of lunar permanently shadowed regions. *Icarus*, 377, 114874.

Cheng, J., Zhang, L., Chen, Q., Hu, X., Cai, J., 2022. A review of visual SLAM methods for autonomous driving vehicles. *Engineering Applications of Artificial Intelligence*, 114, 104992.

Chiodini, S., Giubilato, R., Pertile, M., Salvioli, F., Bussi, D., Barrera, M., Franceschetti, P., Debei, S., 2021. Viewpoint selection for rover relative pose estimation driven by minimal uncertainty criteria. *IEEE Transactions on Instrumentation and Measurement*, 70, 1–12.

Cremons, D. R., 2022. The future of LiDAR in planetary science. *Frontiers in Remote Sensing*, 3, 1042460.

Daftry, S., Chen, Z., Cheng, Y., Tepsuporn, S., Khattak, S., Matthies, L., Coltin, B., Naal, U., Ma, L. M., Deans, M., 2023. LunarNav: Crater-based localization for long-range autonomous lunar rover navigation. *2023 IEEE Aerospace Conference (AERO)*, 1–15.

Ebadi, K., Bernreiter, L., Biggie, H., Catt, G., Chang, Y., Chatterjee, A., Denniston, C. E., Deschênes, S.-P., Harlow, K., Khattak, S. et al., 2023. Present and future of slam in extreme environments: The darpa subt challenge. *IEEE Transactions on Robotics*, 40, 936-959.

Geromichalos, D., Azkarate, M., Tsardoulias, E., Gerdes, L., Petrou, L., Perez Del Pulgar, C., 2020. SLAM for autonomous planetary rovers with global localization. *Journal of Field Robotics*, 37(5), 830–847.

Graeter, J., Wilczynski, A., Lauer, M., 2018. LIMO: LiDAR-monocular visual odometry. *2018 IEEE/RSJ International Conference on Intelligent Robots and Systems (IROS)*, 7872–7879.

Green, D., Sasiadek, J., 1998. Path tracking, obstacle avoidance and dead reckoning by an autonomous planetary rover. *International Journal of Heavy Vehicle Systems*, 5(1), 1–24.

Guo, S., Rong, Z., Wang, S., Wu, Y., 2022. A LiDAR SLAM with PCA-based feature extraction and two-stage matching. *IEEE Transactions on Instrumentation and Measurement*, 71, 1–11.

Harrell, M. J., Schroeder, G. S., Daire, S. A., 2021. Lunar environment, overview. *Handbook of Life Support Systems for Spacecraft and Extraterrestrial Habitats*, 1–23.

Hinduja, A., Ho, B.-J., Kaess, M., 2019. Degeneracy-aware factors with applications to underwater SLAM. *2019 IEEE/RSJ International Conference on Intelligent Robots and Systems (IROS)*, IEEE, 1293–1299.

Huang, R., Wan, G., Zhou, Y., Ye, Z., Xie, H., Xu, Y., Tong, X., 2024. Fast Double-Channel Aggregated Feature Transform for Matching Planetary Remote Sensing Images. *IEEE Journal of Selected Topics in Applied Earth Observations and Remote Sensing*, 17, 9282–9293.

Huang, S.-S., Ma, Z.-Y., Mu, T.-J., Fu, H., Hu, S.-M., 2020. LiDAR-monocular visual odometry using point and line features. *2020 IEEE International Conference on Robotics and Automation (ICRA)*, 1091–1097.

Jia, W., Dafei, L., Ximing, H., Ziqing, C., Qian, X., Xueru, Q., Wenhui, W., 2022. High precision localization of Zhurong rover based on multi-source images. *Journal of Deep Space Exploration*, 9(1), 62–71.

Jun, W. W., Cheung, K.-M., Lightsey, E. G., Lee, C., 2022. A minimal architecture for real-time lunar surface positioning using joint doppler and ranging. *IEEE Transactions on Aerospace and Electronic Systems*, 58(2), 1367–1376.

Kaichang, D., Jia, W., Yan, X., Zhaoqin, L., Wenhui, W., Man, P., Yexin, W., Bin, L., Tianyi, Y., Lichun, L. et al., 2021. Progresses and prospects of environment perception and navigation for deep space exploration rovers. *Acta Geodaetica et Cartographica Sinica*, 50(11), 1457.

Kaichang, D., Wenhui, W., Hongying, Z., Zhaoqin, L., Runzhi, W., Feizhou, Z., 2018. Progress and applications of visual SLAM. *Acta Geodaetica et Cartographica Sinica*, 47(6), 770.

Lacroix, S., De Maio, A., Labourey, Q., Mendes, E. P., Narvor, P., Bissonette, V., Bazerque, C., Souvannavong, F., Viards, R., Azkarate, M., 2020. The erfoud dataset: a comprehensive multi-camera and lidar data collection for planetary exploration. *15th Symposium on Advanced Space Technologies in Robotics and Automation (ASTRA)*.

Lai, J., Xu, Y., Bugiolacchi, R., Meng, X., Xiao, L., Xie, M., Liu, B., Di, K., Zhang, X., Zhou, B. et al., 2020. First look by the Yutu-2 rover at the deep subsurface structure at the lunar farside. *Nature Communications*, 11(1), 3426.

Li, H., Tian, B., Shen, H., Lu, J., 2022. An intensity-augmented LiDAR-inertial SLAM for solid-state LiDARs in degenerated environments. *IEEE Transactions on Instrumentation and Measurement*, 71, 1–10.

Li, N., Yao, Y., Xu, X., Peng, Y., Wang, Z., Wei, H., 2024. An efficient LiDAR SLAM with angle-based feature extraction and voxel-based fixed-lag smoothing. *IEEE Transactions on Instrumentation and Measurement*, 73, 1-13.

Maimone, M., Cheng, Y., Matthies, L., 2007. Two years of visual odometry on the mars exploration rovers. *Journal of Field Robotics*, 24(3), 169–186.

Meng, L. B., Ye, C., Lin, W. Y., 2022. A tightly coupled monocular visual LiDAR odometry with loop closure. *Intelligent Service Robotics*, 15(1), 129-141.

Sasaki, T., Otsu, K., Thakker, R., Haesaert, S., akbar Aghamohammadi, A., 2020. Where to map? Iterative rover-copter path planning for Mars exploration. *IEEE Robotics and Automation Letters*, 5(2), 2123–2130.

Shan, T., Englot, B., 2018. Lego-loam: Lightweight and ground-optimized lidar odometry and mapping on variable terrain. *2018 IEEE/RSJ International Conference on Intelligent Robots and Systems (IROS)*, IEEE, 4758–4765.

Sicong, L., Xiaohua, T., Shijie, L., Huan, X., Hui, Z., Dayong, L., Xiong, X., Zhen, Y., Chao, W., Xianglei, L., 2022. Topography modeling, mapping and analysis of China’s first Mars mission Tianwen-1 landing area from remote sensing images. *Journal of Deep Space Exploration*, 9(3), 338–347.

Tian, Z., Zhang, H., Hu, Q., 2024. Global localization technology of Lunar rover by horizon line matching. *IEEE Transactions on Aerospace and Electronic Systems*, 1-13. early access.

Wan, G., Huang, R., Xu, Y., Ye, Z., You, Q., Yan, X., Tong, X., 2025. Efficient Phase Congruency-Based Feature Transform for Rapid Matching of Planetary Remote Sensing Images. *IEEE Geoscience and Remote Sensing Letters*, 22, 1–5.

Wang, Y., Zhang, W., An, P., 2017. A survey of simultaneous localization and mapping on unstructured lunar complex environment. *AIP Conference Proceedings*, 1890(1), 030010.

Wu, Z., Yue, Y., Wen, M., Zhang, J., Yi, J., Wang, D., 2021. Infrastructure-free hierarchical mobile robot global localization in repetitive environments. *IEEE Transactions on Instrumentation and Measurement*, 70, 1–12.

Xia, Y., Gladkova, M., Wang, R., Li, Q., Stilla, U., Henriques, J. a. F., Cremers, D., 2023. Casspr: Cross attention single scan place recognition. *Proceedings of the IEEE/CVF International Conference on Computer Vision (ICCV)*, 8461–8472.

Xia, Y., Xu, Y., Li, S., Wang, R., Du, J., Cremers, D., Stilla, U., 2021. Soe-net: A self-attention and orientation encoding network for point cloud based place recognition. *Proceedings of the IEEE/CVF Conference on Computer Vision and Pattern Recognition (CVPR)*, 11348–11357.

Xie, H., Zhang, D., Wang, J., Zhou, M., Cao, Z., Hu, X., Abusorrah, A., 2023. Semi-direct multimap SLAM system for real-time sparse 3-D map reconstruction. *IEEE Transactions on Instrumentation and Measurement*, 72, 1–13.

Yang, P., Xie, L., Liu, J., 2014. Simultaneous celestial positioning and orientation for the lunar rover. *Aerospace Science and Technology*, 34, 45–54.

Ye, P., Huang, R., Xu, Y., Li, W., Ye, Z., Tong, X., 2025. 3D Morphometry of Martian Craters from HRSC DEMs Using a Multi-Scale Semantic Segmentation Network and Morphological Analysis. *Icarus*, 426, 116358.

Zhang, J., Kaess, M., Singh, S., 2016. On degeneracy of optimization-based state estimation problems. *2016 IEEE International Conference on Robotics and Automation (ICRA)*, IEEE, 809–816.

Zhang, J., Kaess, M., Singh, S., 2017. A real-time method for depth enhanced visual odometry. *Autonomous Robots*, 41(1), 31-43.

Zhang, J., Singh, S., 2015. Visual-LiDAR odometry and mapping: low-drift, robust, and fast. *2015 IEEE International Conference on Robotics and Automation (ICRA)*, IEEE, 2174–2181.

Zhen, W., Scherer, S., 2019. Estimating the localizability in tunnel-like environments using lidar and uwb. *2019 International Conference on Robotics and Automation (ICRA)*, IEEE, 4903–4908.

Zhu, J., Li, H., Zhang, T., 2023. Camera, LiDAR, and IMU based multi-sensor fusion SLAM: A survey. *Tsinghua Science and Technology*, 29(2), 415–429.